1995ApJ...439..365S

THE ASTROPHYSICAL JOURNAL, 439:365–380, 1995 January 20

YOUNG OXYGEN-RICH SUPERNOVA REMNANTS. I. OBSERVATIONS OF THREE SOUTHERN REMNANTS

RALPH S. SUTHERLAND[1] AND MICHAEL A. DOPITA[2]
Received 1993 October 29; accepted 1994 June 10

ABSTRACT

Narrowband imaging and two-dimensional spectrophotometery are combined in a series of observations of N132D, a young, oxygen-rich supernova remnant in the Large Magellanic Cloud. Comparison spectra of two galactic remnants, Pup A and SNR G292.0+1.8 are also examined. The observations permit the determination of some important physical parameters of the N132D remnant in particular. An expansion age of 2350 ± 520 yr is obtained, significantly greater than the ~1300 yr obtained by Lasker (1980). Estimates of the densities and temperatures in the observed oxygen-rich material are made on the basis of simple homogeneous slab models. The models indicate that such simple models are unlikely to be appropriate; nevertheless they do highlight the difficulties of interpretation when the diagnostic plot trends lie in similar directions to that expected from reddening effects. Line fluxes are given in raw form, and estimates of the reddening that may be applicable are given.

This forms the first paper in a short series, in the second paper an excitation mechanism for the oxygen-rich material, based on an R-type ionization front model, is presented.

Subject headings: gamma rays: bursts — methods: statistical

1. INTRODUCTION

The interest in the small class of young, oxygen-rich supernova remnants (OSNRs) lies in the unique opportunity that they provide in allowing us to examine directly the internal, nuclear-processed material of massive stars. Considered here are three southern sky remnants: SNR G292.0+1.8 and Pup A, both galactic remnants, and N132D in the Large Magellanic Cloud (LMC).

1.1. *SNR G292.0+1.8*

The remnant SNR G292.0+1.8 (MSH 11−54) is a center-filled radio remnant, and it has been suggested in the past that it may be "plerionic" or pulsar powered, similar to the Crab Nebula (Lockhart et al. 1977; Goss et al. 1979). However, it has a radio spectral index of −0.37, similar to a normal shell SNR and in contrast to the flat spectrum of a synchrotron nebula (Clark, Tuohy, & Becker 1980). It is a strong X-ray source like the rest of the OSNRs, a result which is not unexpected if the hot plasma consists largely of heavy elements. The X-ray data from the *Einstein* solid-state spectrometer (SSS) instrument shows clear evidence of magnesium, silicon, and sulfur emission in the hot phase of the remnant.

The distance to this remnant, which lies very close to the Galactic plane, has been estimated at 3.6 kpc by *IRAS* line-of-sight dust (Braun et al. 1986). It clearly heavily reddened. However, normal optical emission line methods using Balmer-line decrements are useless in this case. A reddening of $E(B-V) = 0.9$ has been quoted by Goss et al. (1979), which would be consistent with the estimated distance and position in the galaxy. The true reddening remains very uncertain.

At the estimated distance, the physical size of the centrally emitting region is approximately 2 pc, direct evidence that this is a young SNR. It was probably a historical event, with ages estimated in the range 1500–2000 yr, but presumably the southerly declination and high reddening prevented it being noticed by northerly civilizations.

The optical spectrum only displays forbidden oxygen and neon lines (Dopita & Tuohy 1984). There is no sign of the heavier elements such as argon or sulfur in the optical spectrum. There has been a suggestion that the X-ray emission is in fact toroidal in geometry, and there does appear to be growing evidence for the nonspherical nature of the OSNR outbursts, possibly favoring the equatorial plane.

1.2. *Pup A*

Pup A is becoming an increasingly well studied remnant (cf. Arendt, Dwek, & Petre 1991, and references therein). Since the identification by Baade & Minkowski (1954) of some bright nebula condensations with the radio source Pup A, the remnant was generally held to be a middle-aged, fairly normal galactic remnant. The delicate sheets and filaments of other old remnants are not present, rather the optical nebulosity occurs in a collection of individual knots scattered across the 60′–80′ covered by this remnant. These knots display a range of spectra, and some are noted for the particularly strong emission of [N II]. The [N II] λ6584 emission is between 10 and 20 times Hα in some cases (Dopita, Mathewson, & Ford 1977; Danziger 1983).

There is also optical evidence that the remnant contains clumped and diffuse coronal gas with [Fe XIV) λ5303 emission detected by Clark et al. (1979). The [Fe XIV] λ5303 corresponds roughly with the overall diffuse X-ray emission, although much of the emission is very weak. Pup A is typical of OSNRs in being a bright X-ray source. It has been observed extensively in X-rays, including spectrally by Winkler et al. (1981) and imaging by Petre et al. (1982). The X-ray observations have been used to place constraints on the density and temperature of the hot medium in the SNR, and hence the pressure domain of the remnant including any embedded knots.

---

[1] Joint Institute for Laboratory Astrophysics, University of Colorado and National Institute of Standards and Technology, Campus Box 440, Boulder, CO 80309.

[2] Mount Stromlo and Siding Spring Observatories, Australian National University, Private Bag, Weston Creek Post Office, ACT 2611, Australia.

The status of this remnant was reevaluated with the discovery by Winkler & Kirshner (1985) of rapidly moving knots of oxygen-rich material. The bright "Omega" filament displays the typical OSNR forbidden oxygen and neon emission spectrum. Other fainter rapidly moving knots were also detected. By 1988, using plates taken in 1978 and 1986, proper motions were measured for individual knots giving space velocities around 1500–3000 km s^{-1} (Winkler et al. 1988). This is somewhat slower than similar knots observed in Cas A knots (cf. Kamper & van den Bergh 1976; van den Bergh & Kamper 1983, 1985; hereafter K&B, referring to all the works together), suggesting that deceleration has occurred. The expansion age they derived, 3700 ± 300 yr, makes Pup A the oldest of the known OSNRs. Arendt et al. (1991) favor an even greater age, about 6000 yr. The distance has been estimated between 2 and 4 kpc, although the work by Arendt et al. supports the shorter distances. The reddening is again uncertain and has been estimated at $A_v = 1.5$ by Winkler et al. (1988).

The oxygen-rich knots contain the usual oxygen-neon mixture. Some [S II] λλ6717+31 emission is seen in other filaments, but the same knots also display strong [N II] emission, making the possibility of a deep stellar origin for the observed sulfur unlikely, unless extensive mixing of the deep layers and the outer envelope has occurred.

1.3. *N132D*

When placed at the distance of the LMC, the physical extent of 30 pc makes N132D an ideal target for typical modern detector systems (both imaging and spectral). The apparent diameter is about 2′ for N132D. This remnant displays the characteristic properties of the OSNRs with rapidly moving oxygen-rich material, and slow-moving "quasi-stationary flocculi" (QSFs) analogous to the Cassiopeia A structures described by K&B. For the present discussion, the distance to the LMC has been taken to be 49.4 kpc based on the review by Feast & Walker (1987).

One of the first remnants identified in the LMC (Westerlund & Mathewson 1966), N132D has high surface brightness in both the optical and radio bands. This OSNR is also one of the brightest X-ray sources in the LMC as a whole. As much as 20% of the X-ray luminosity may come from O VIII line emission (Winkler et al. 1979). The optical structure of this remnant is one of a series of three roughly circular structures. There is an outer, diffuse, low-excitation nebulosity with a diameter of about 80 pc (Lasker 1978). What is commonly regarded as the remnant proper is a roughly circular structure about 32 pc in diameter. Within this shell lies a complex of knots in a region about 6–12 pc across, containing slow-moving material and the fast oxygen-rich knots. The X-ray and optical morphology of the 32 pc structure are similar; however, the radio diameter of Mathewson & Clark (1973) corresponds only to the inner 6 pc region (where the oxygen-rich knots are also observed). More recent Australia Telescope 6 cm radio observations by Dickel & Milne (1993) do show the 32 pc remnant extent; however, the detailed structure in the radio image does not correlate well with the optical structure. The *Einstein* X-ray spectrum of Clark et al. (1982) also shows the presence of the heavier elements Mg, Si, and S at mildly supersolar ratios, while the optical spectra of the oxygen-rich knots show only oxygen and neon.

The optical studies carried out by Lasker (1978, 1980) used photographic imaging and spectrophotometry. The results were interpreted in terms of an expanding circular ring of fast-moving oxygen knots, with a diameter of ~6 pc. The study by Hughes (1987) suggests that the supernova event occurred in an evacuated cavity. The homogeneous Sedov solution to the X-ray data suggests an age of 4000–7000 yr, compared to the expansion age of the rapidly moving oxygen-rich knots of ~1300 yr derived by Lasker (1980) for the 6 pc ring. These ages can be somewhat reconciled by assuming that the remnant is expanding into a very low density cavity. Such a cavity may be produced by the wind-blown bubble mechanism commonly seen with Wolf-Rayet (W-R) stars, recalling once more the frequently invoked relationship between OSNRs and W-R stars. The ring of diffuse and relatively faint H II emission seen around N132D (Lasker 1978) at a diameter of about 80 pc is a typical size for a W-R or O star wind bubble.

The spectra of the fast-moving knots of N132D show lines of forbidden oxygen and neon transitions. The [O II] λλ7320+30 lines are relatively weak compared to some knots in Cas A, which may indicate a lower knot intensity. No rapidly moving sulfur, argon, or calcium emission has been detected to date (including the present work). In a search for rapidly moving knots rich in sulfur, Lasker (1988, 1991) could only place upper limits on the sulfur abundances, since sulfur lines were not detected. The implications of the are unclear however, and interpretation is difficult as the layer that contains the heavier elements is relatively small compared to the oxygen-neon layer in the typical 25 $M_{\odot}$ models. The physics of the explosion event, especially the Rayleigh-Taylor instabilities, such as are believed to have occurred in SN 1987A (i.e., Fryxell, Müller, & Arnett 1991), may affect the detectability. For instance if the sulfur-containing material is particularly dense, or not currently being excited, then it may be present but not detectable. Sulfure is detected in the X-ray observations (Clark et al. 1982) but at levels only marginally enhanced over solar ratios.

If the outer diameter ~32 pc represents the position of the primary blast wave after only 1300 yr, then the front is still traveling at around 10,000 km s^{-1} and it would seem that significant deceleration has not yet occurred. It is therefore uncertain whether a reverse shock from the blast wave–interstellar medium (ISM) interface has yet built up as the main front begins to "snow-plow" into the surrounding ISM. Other reflected shocks from the immediate circumstellar medium do presumably exist, however. Such shocks could excite the oxygen-rich material. The shock interaction model is supported by the correlation between the radio emission being strongest in the central 6–12 pc region where the oxygen-rich material is observed, even though the correlation on subparsec scales is not good.

The details of the common observations and data reduction methods used on all the remnants are described in § 2. Details of the results and interpretation on a remnant-by-remnant basis are given in subsequent sections.

2. OBSERVATIONS OF THREE SOUTHERN REMNANTS

The selection of the targets for this study was based both on the perceived areas where the existing literature data can be improved upon, and on the geographical location of the available telescopes. This led to the selection of three of the southern remnants which have properties which make them suited to the available observational tools. Limited optical spectrophotometric data already exist in the literature for N132D, Pup A, and SNR G292.0+1.8 (i.e., Lasker 1978, 1980; Goss et al. 1979; Dopita & Tuohy 1984; Danziger & Dennefeld 1976a. b; Danziger & Liebowitz 1985; Winkler & Kirshner 1985). The aim here is to go back and make a more detailed study. The other southern remnants: SNR 0540−69.3 (Dopita & Tuohy 1984; Kirshner et al. 1989) and SNR E102.2−7219 (Dopita & Tuohy 1984; Blair et al. 1989) already have good published spectra which could not be improved upon by the techniques employed here.

The Pup A observations were intended to provide new data on known oxygen-rich material and to search for new oxygen-rich knots using a [O III]-filtered Schmid plate in conjunction with other photographic, red [N II] + Hα materials. In addition, a global spectrum of the remnant SNR G292.0+1.8 was obtained. The N132D remnant provides an opportunity for a more detailed study, and a two-dimensional spectrophotometric technique was applied to obtain both velocity field information of the oxygen-rich material as well as spectra of individual knots. N132D was the subject of the narrow-band imaging.

2.1. *Spectrophotometry*

All the spectrophotometry in this work was carried out using the double-beam spectrograph (DBS) (Rodgers, Conroy, & Bloxham 1988a) on the Australian National University's 2.3 m Advanced Technology Telescope (ATT) at Siding Spring Observatory. The DBS red and blue beams are each detected with wavelength-optimized photon counting arrays (PCAs) (Rodgers et al. 1988b). Using the 300 and 316 lines mm^{-1} gratings, a spectral range of 3300–8000 Å is covered at approximately 1.5 Å per pixel. The slit width of 1″.5–2″ degraded the FWHM resolution to around 6 Å resolution overall.

Single-slit exposures of 1500 s were taken of white dwarf flux standards, to provide relative flux calibration. The standards used were L745−46A and Wolf 485 from the list of Oke (1974). Spectra of standards were obtained twice per night. The observations of the targets used wide slit settings. However, the standard stars required narrow slits with defocusing to prevent detector count-rate saturation, and this prevented accurate absolute calibration. The defocusing of the narrow-slit observations of the standards also compensated for the normal atmospheric dispersion errors usually encountered with narrow-slit observations. The optical design of the spectrograph does not produce significant vignetting in the cameras so that wavelength dependent effects of defocusing are negligible.

Quartz flat fields were taken at low count rates with exposures of up to 30,000 s. For these, the grating angles were changed to give a more even illumination of the blue PCA detectors. The flat fields were used to largely eliminate a number of large-scale detector defects, dust contamination, and to a lesser extent the local up-down noise of the detectors. Some defects due to fiber-packing discontinuities in the optical fiber boules varied slightly with time and could not be eliminated by flat-fielding techniques. The main effect of these packing errors is that emission lines sometimes cross a discontinuity and apparently shift suddenly in wavelength. These discontinuous shifts could not be eliminated in the wavelength calibration procedure as the calibration uses polynomial fits which cannot reproduce them. Occasionally, these discontinuities produce a ridge in the final processed spectra that appear as weak emission lines. When such features have occurred in the final spectra presented in Figures 1–3, the spurious lines are marked as " PCA."

The spectrophotometry was reduced in the standard way using the NOAO packages in IRAF version 2.9. Individual observations frequently resulted in several emission knot detections along a single slit. To make the strip extraction of the knot spectra more reliable, a slit-axis calibration was taken. The calibration was in the form of an aperture plate of artificial stars along the slit axis. The "stars" were placed with 2 mm spacings above and 3 mm spacings below the central position so that the orientation solution was included in the scale-fitting procedure, since the red frames from the PCAs are inverted vertically compared to the blue frames in the raw data. The calibration plate was illuminated using the quartz flat-field lamp. The artificial star images were then fitted using normal arc identification methods, along the slit axis. The physical plate scale was 4″.964 per mm at the plate plane in the Naysmith position of the DBS. The slit scales vary between 0″.663 per pixel and 0″.639 per pixel depending on the individual PCA chips. The resulting slit fit was combined with the He/Ne/Ar arc fits for the dispersion axis to make a two-dimensional distortion correction in one operation. Once the distortions were corrected, all the PCA frames were standardized to 1.5 Å per pixel along the dispersion axis and 0″.665 per pixel along the slit axis.

Background sky subtraction was carried out on the distortion-corrected long-slit spectra before aperture strips were extracted. This was necessary, since often the emission observed was so extended that true sky values were only available near the outer edges of the data frames, and apertures near the center could not define nearby sky values for subtraction during the extraction procedure. In the case of the N132D observations the series of long-slit observations thus corrected and background subtracted were also stacked into a λ-x-y data cube, resulting in 1.5 Å × 2″.5 × 0″.665 volume elements.

Individual spectra were then extracted as simple summed rows of pixels, without using the automatic aperture-tracing facilities, which are not useful for emission-line objects with weak or no continuum. The rows to be summed were chosen interactively, using the apertures defined by the available imaging and velocity map information (see §§ 3.1.2 and 4). In most cases, however, the individual knots were clearly isolated and extraction was straightforward. Final line fluxes were interactively measured using the IRAF SPLOT package.

In the extraction of individual apertures in the N132D data, spectra were extracted from one, two, or sometimes three slit positions and co-added. This procedure involved adding several spectra from different apertures along planes of the data cube. This further prevented absolute spectrophotometry, although relative fluxes were preserved.

The measured lines were all well within the detector range and away from both detector edges and the regions affected by the dichroic filter system. The final relative spectrophotometry was repeatable on the 10%–15% level or better for Hβ or [O III] λ4959 when observations from different nights were compared. This error is largely due to high thin clouds on some nights and difficulties in eliminating count-rate saturation in the PCA detector system. The I_{5007}/I_{4959} ratio is constrained by atomic theory to be 1:0.347. In the tables of flux ratios below, the observed ratio is given and the general agreement with this ratio indicates that serious saturation in the [O III] λ5007 line has not occured.

2.1.1. *Three-dimensional Spectrophotometry*

The precision tracking and slit positioning of the 2.3 m ATT permitted the accurate offsetting of the 6′ DBS slit in a regular grid. With the relatively poor seeing of 2″ or more, offsets of 2″.5 east-west were taken with the 2″ slit in a north-south orien-

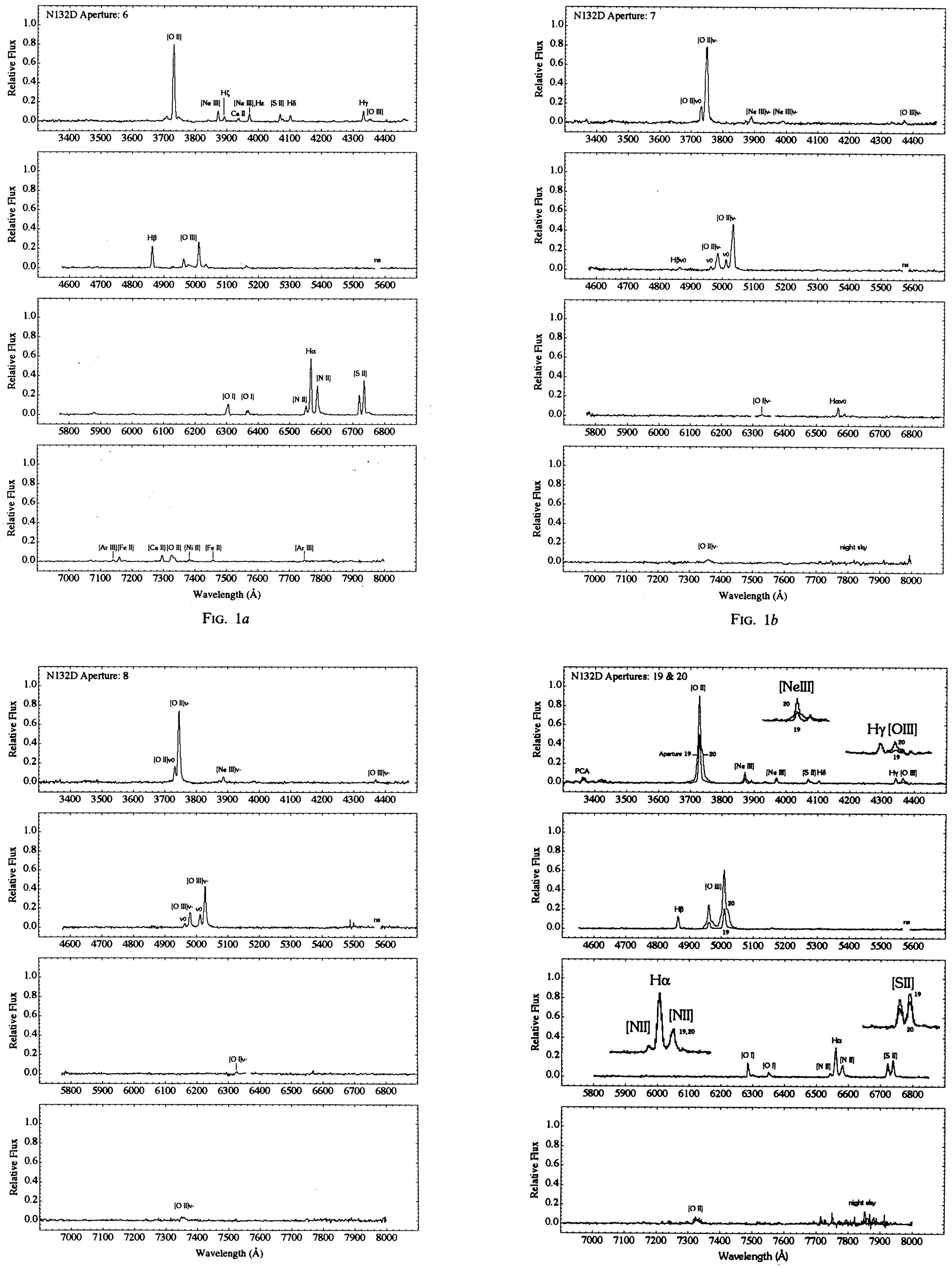

FIG. 1*a*

FIG. 1*b*

FIG. 1*c*

FIG. 1*d*

FIG. 1.—N132D: (*a*) aperture 6, (*b*) aperture 7, (*c*) aperture 8, (*d*) apertures 19 and 20

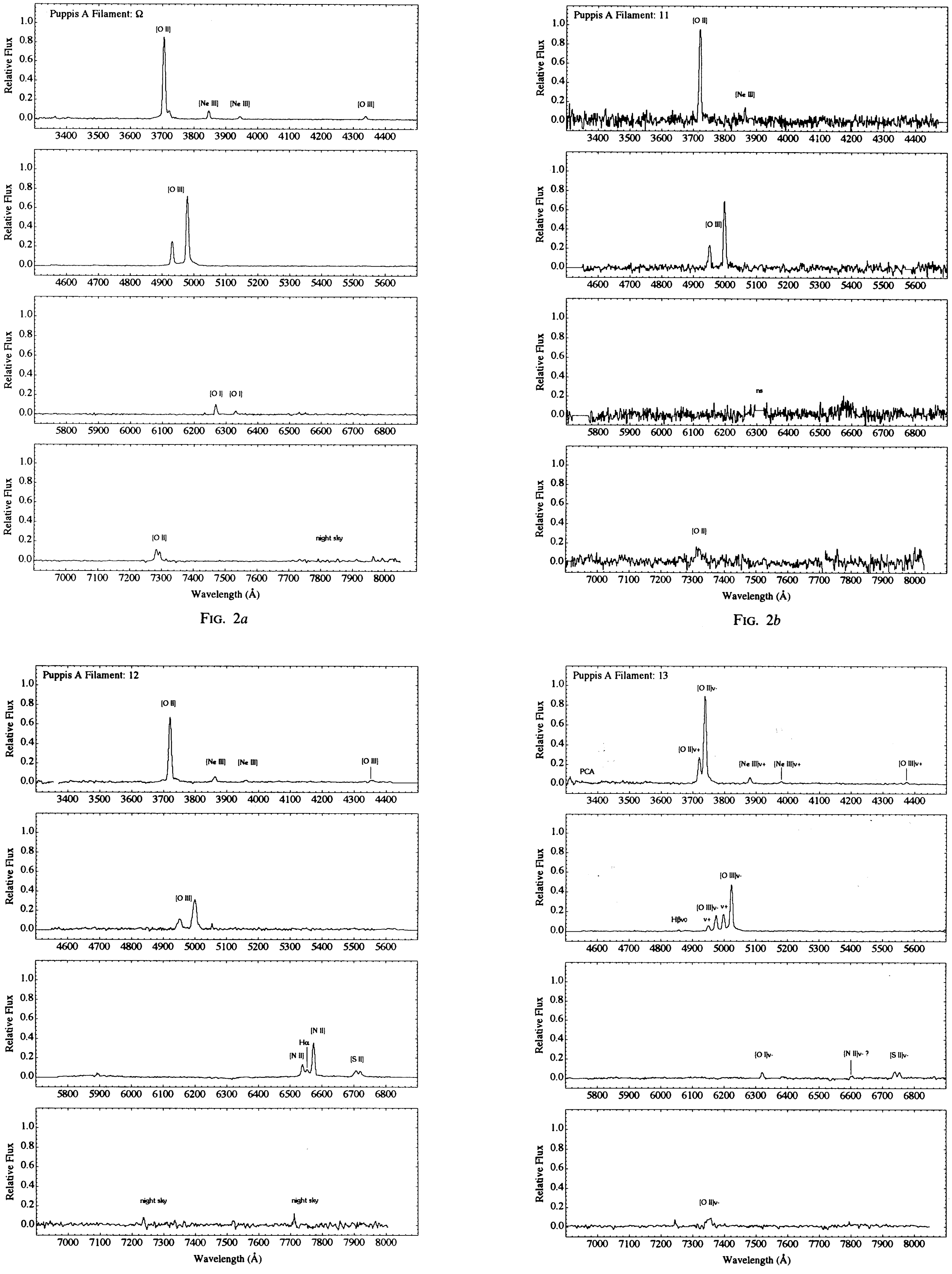

FIG. 2*a*

FIG. 2*b*

FIG. 2*c*

FIG. 2*d*

FIG. 2.—Pup A: (*a*) "Omega" filament, (*b*) aperture 11, (*c*) aperture 12, (*d*) aperture 13

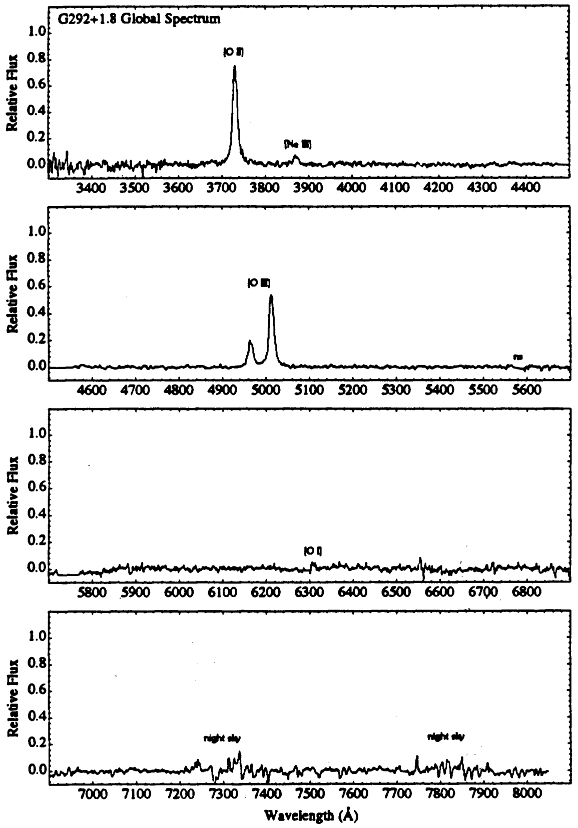

FIG. 3.—SNR G292.0+1.8 global spectrum

tation. A standard position star at $5^{\rm h}25^{\rm m}06^{\rm s}.625-69^\circ37'38''.325$ (J2000.0) (Mathewson et al. 1983) was used to maintain accuracy during the course of the observations, by resetting to that position and making relative offsets from there to the desired slit position. In this way two-dimensional spectrophotometric observations resulting in a λ-x-y data cube of the remnant were taken and then reduced as described above.

From the data cube, a section containing all the [O II] $\lambda\lambda3727$ emission (the doublet is unresolved in these observations) was taken and a velocity map was constructed from this single line. The isolated nature of this emission prevents the ambiguities that are inherent in an [O III] $\lambda5007$ line observation, where high velocities can cause confusion with [O III] $\lambda4959$ emission.

2.1.2. *Narrowband Imaging*

Narrowband imaging was carried out using the Anglo-Australian Observatory (AAO) 3.9 m Anglo-Australian Telescope (AAT) 1991 February 16 and 17. The TAURUS II instrument (Atherton et al. 1982) was mounted at Cassegrain focus and used without the Fabry-Perot capability. The instrument functioned essentially as a focal reducer, giving an effective ratio of f2.2, and tiltable filter holder. The 100 mm and 76 mm emission-line filters were placed above the focal plane in the primary f8 beam, so that bandpass broadening due to off-axis rays was unimportant. Red and green continuum filters with diameters of 76 mm were placed at the pupil plane. This meant that only the central 50 mm of these filters were used, avoiding the filter edges which were becoming somewhat degraded due to moisture damage.

Exposures of 1000 s were taken with a 1024 × 1024 pixel Thompson CCD. The resulting resolution was $0''.467$ per pixel in an $\sim 8'$ field. Atmospheric seeing conditions during the observations were measured at $2''.5$. Narrow-band interference filters with bandpasses of 5020 ± 20 Å and 6565 $\pm$ 7.5 Å were used for [O III] and Hα emission, respectively. The off-line green and red continuum filters had bandpasses of 5057 $\pm$ 21 Å and 6626 $\pm$ 27.5 Å. The continuum images were subtracted from the emission-line images after registration and normalization to minimize the residual stellar images. The CCD image reduction was done with the IRAF data reduction facility, using standard reduction methods.

2.2. *Observation Log*

The observing log, giving dates, integration times, and slit positions for all observations are given in Tables 1 and 2.

2.3. *Spectra, Line Fluxes, and Ratios*

Spectra for some positions of particular interest are plotted in Figures 1–3. The spectra are plotted with rectilinear steps at the actual pixel resolution, and no smoothing has been used. Defects, such as night-sky emission that subtracted poorly or defects in the PCA, are noted. In the spectra up to three velocity components were observed, so components have been labeled with $v+$, $v0$, and $v-$ representing blueshifted, local SNR rest frame, and redshifted material, respectively.

The measured line ratios relative to $I_{5007} = 1.00$ are given in Tables 3 and 4. In many cases, particularly the N132D observations, confusion and blending of lines prevented quantitative measurement of fluxes in some apertures. The tables also include line ratios between the various lines that are in subsequent analysis. The $v+$, $v0$, and $v-$ notation is used in the N132D tables. In the Pup A observations, where some slit positions covered knots of different composition, they are differentiated by the labels *a*, *b*, and *c* as necessary.

TABLE 1

OXYGEN-RICH FILAMENT OBSERVATIONS

N132D OXYGEN-RICH	COORDINATES (J2000.0)[a] R.A.	Decl.	EXPOSURE[b] (s)
4	$05^{\rm h}25^{\rm m}02^{\rm s}.4$	$-69^\circ38'50''.1$	1500 (1)
5	05 25 04.3	−69 38 37.8	1500 (1)
6[c]	05 25 01.5	−69 38 41.6	3000 (2)
7	05 25 00.7	−69 38 35.0	4500 (3)
8	05 25 00.6	−69 38 28.0	4500 (3)
9	05 25 01.9	−69 38 23.7	3000 (2)
10	05 25 02.3	−69 38 31.2	3000 (2)
11	05 25 03.6	−69 38 30.3	3000 (2)
12	05 25 03.3	−69 38 23.8	3000 (2)
14	05 25 06.0	−69 38 28.0	3000 (2)
15	05 24 59.4	−69 38 48.1	1500 (1)
16	05 25 00.7	−69 37 45.8	4500 (3)
19[d]	05 25 03.7	−69 38 13.5	4500 (3)
20	05 25 05.3	−69 38 12.1	4500 (3)

NOTES.—All observations were made in 1989 December at P.A. 180°.

[a] Astrometry for individual filaments using narrowband CCD imaging from 1991 February. See Fig. 9.

[b] Total exposure, and number of contributing slit positions in parentheses.

[c] Normal composition filament for comparison in Fig. 1*a*.

[d] Normal composition filament subtracted from filament 20 spectrum in Fig. 1*d*.

1995ApJ...439..365S

1995ApJ...439..365S

TABLE 2

GALACTIC OXYGEN-RICH FILAMENT OBSERVATIONS

A. PUP A

FILAMENT	COORDINATES (J200.0)[a] R.A.	Decl.	P.A.	DATE	EXPOSURE[b] (s)
Omega......	$08^{\rm h}22^{\rm m}42^{\rm s}.2$	$-42^\circ51'55''.2$	226°	1989 Dec 1990 Mar 1991 Jan	7000 (3)
O2	08 24 15.9	−42 58 02.4	135	1990 Mar	3000 (1)
O3	08 22 50.3	−42 44 37.0	130	1990 Mar	3000 (1)
O4	08 22 39.1	−42 42 50.4	90	1989 Dec	2000 (1)
O5	08 24 18.8	−42 55 02.5	90	1990 Mar	3000 (1)
O11	08 23 28.7	−42 52 22.2	135	1990 Mar	3000 (1)
O12	08 22 55.0	−42 55 22.8	135	1989 Dec	2000 (1)
O13	08 23 20.0	−42 54 42.9	135	1990 Mar	3000 (1)

B. SNR G292.0+1.8

FILAMENT	COORDINATES (J1950.0)[c] R.A.	Decl.	P.A.	DATE	EXPOSURE (s)
Whole	$11^{\rm h}22^{\rm m}32^{\rm s}.73$	$-58^\circ59'12''.9$	270°	1990 Mar	3000 (1)

[a] Astrometry for individual filaments using [C III] Schmidt plate of Dopita 1983.

[b] Total exposure, and number of exposures in parentheses.

[c] DBS slit position, centered on filaments. 2.3 m ATT console readout, accurate to ~1′.

3. N132D

3.1. *Images*

Narrowband images in both Hα and [O III] lines were taken of N132D using a large-format CCD on the 3.9 m AAT. By also taking images with narrowband filters in adjacent continuum, the relatively crowded background stellar field has been accurately subtracted. The pure emission Hα and [O III] images can then be combined to differentiate the filaments into normal and oxygen-rich classes. While the [O III] narrowband filter excluded the highest velocity material with velocity Doppler shifts of more than ±25 Å, the images clearly show that the well-known arc features in the remnant described by Mathewson et al. (1983) are not entirely oxygen-rich material. Much of the arc material is of more or less normal composition.

The two-dimensional spectrophotometry, resulting in a velocity map of the innermost regions, demonstrates that the highest velocity material, which is excluded from the narrowband images, appears to fill the region interior to the inner arcs. Material is found inside the circular "ring" found by Lasker (1980). This may be a result of the higher resolution achieved here, being 16 times the spatial resolution with elements of $0''.65 \times 2''.5$, compared with $2''.4 \times 7''$ in the previous work. The circular geometry found by Lasker may be at least partially a selection effect, where the most extended oxygen-rich material has been neglected. The analysis by Lasker excluded slow material within 600 km $\rm s^{-1}$ of the nominal rest velocity. This would automatically exclude the most peripheral material, which will be traveling across the line of sight. In addition, the analysis neglected some observed emission outside the ring which showed both blue and redshifted material. This important feature is discussed in some detail below.

3.1.1. *Narrowband Imaging*

The pure emission line images produced as described above are shown as gray-scale images in Figures 4 and 5. Contour plots have been overlaid to emphasize the image features.

A composite image with the [O III] image in green and the Hα image in red is reproduced in color in Figure 6 (Plate 10). The composite shows the overall excitation level of the remnant compared to the adjacent red H II region to the south which is part of the outer 80 pc halo. The emission of the rapid oxygen-rich filaments that are slow or redshifted is able to pass the filter, and appear as pure green knots. Blueshifted material will be excluded by the bandpass which is centered at 5020 Å.

The images are in broad agreement with the images of Mathewson et al. (1983) and Lasker (1980), however the scale bar in the Mathewson et al. atlas appears to be in error. Unfortunately, the poor seeing conditions prevented a detailed comparison with the earlier epoch observations. Any changes in

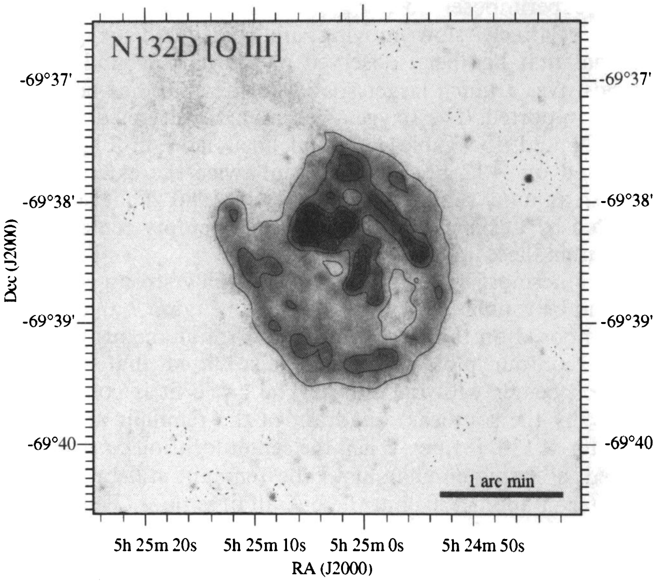

FIG. 4.—N132D [O III] gray-scale image. This continuum-subtracted image shows [O III] emission from both oxygen-rich and normal composition material. Contours are overlaid to highlight features.

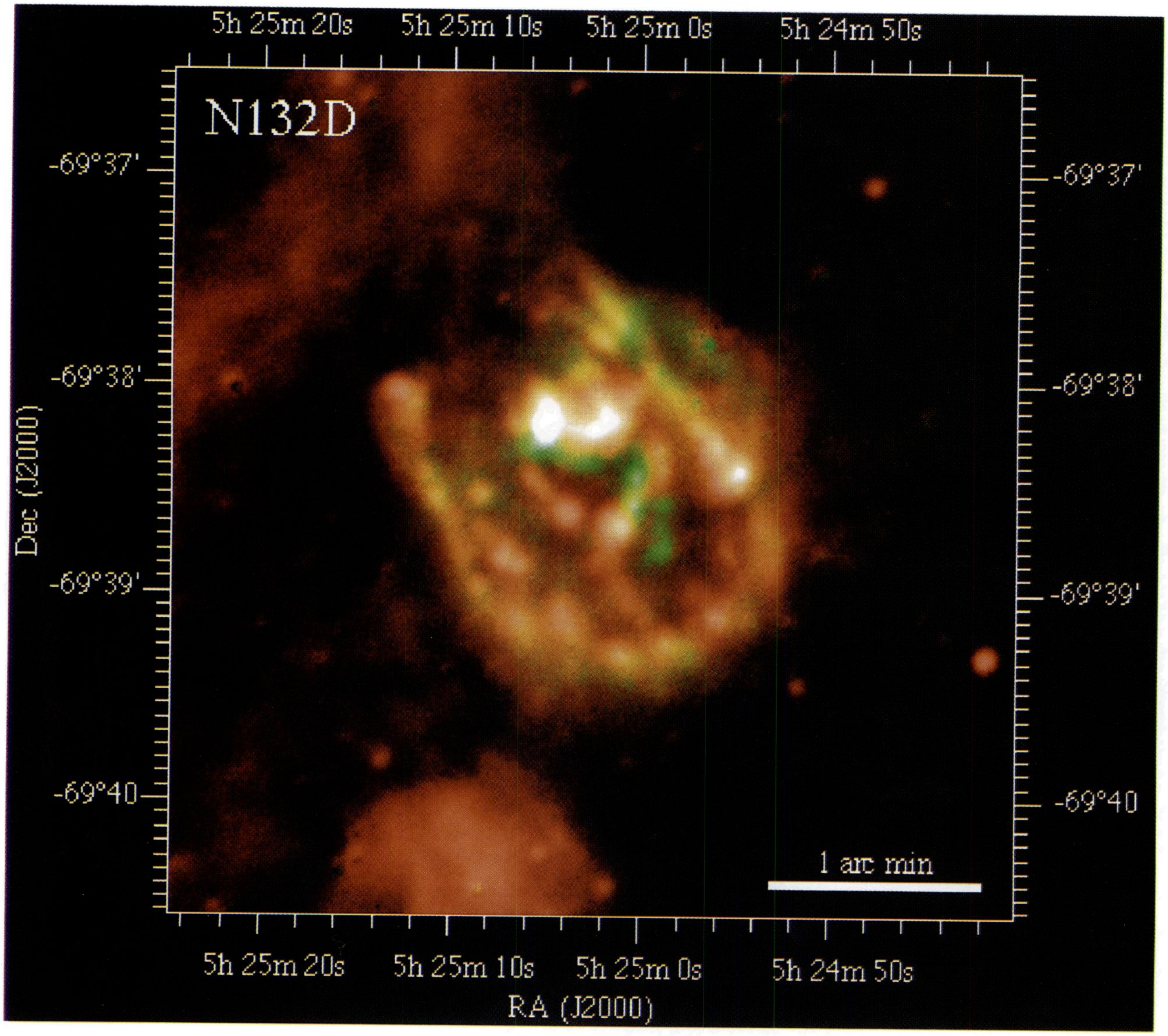

FIG. 6.—This image is a composite narrowband, continuum-subtracted CCD image of the SNR N132D. It consists of an Hα emission image in red, and a forbidden [O III] λ5007 image in green. See text for details.

SUTHERLAND & DOPITA (see 439, 371)

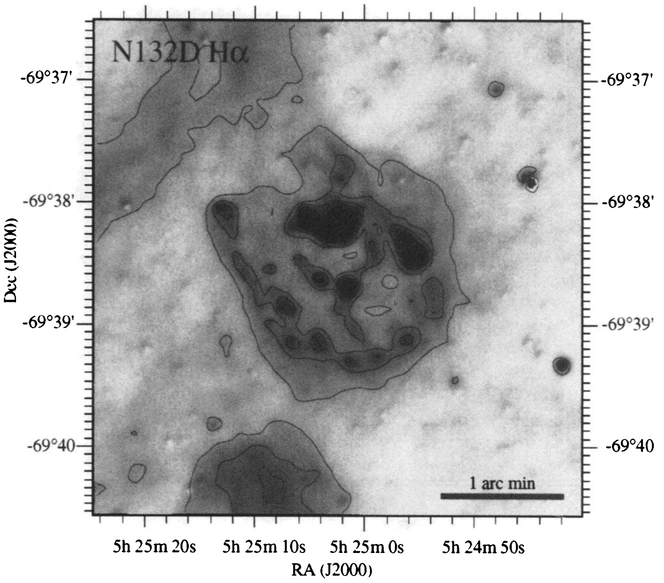

FIG. 5.—N132D Hα gray-scale image. This continuum-subtracted image shows the normal composition material in the remnant. Contours are overlaid to highlight features.

the emission due to appearance or disappearance of filaments similar to the changes noted in Cas A by K&B were not detectable.

The accurate continuum subtraction has brought out fainter diffuse emission throughout the remnant. The remnant also has a more nearly circular appearance than in the previous works, due to a faint emission region in the northwest of the remnant. The oxygen-rich material is located in the central ~25″ radius of the remnant, along with material which displays emission spectra consistent with shock-excited material of more normal cosmic abundances (see § 3.2 and aperture 6 in Fig. 1*a*). The oxygen-rich material appears in these images in the southwest regions of the central complex. The large bright knot in the northeast, later defined as aperture 20 on Figure 9, also contains oxygen-rich emission, but it is less clear as it is largely superimposed on a bright normal composition knot.

The relatively slow moving and redshifted oxygen-rich material that has been observed in the narrowband images extends over a much larger spatial region than has been previously reported. The oxygen-rich material detected in apertures 20 and 15 (Table 1, and defined later in Fig. 9) are separated by ~12 pc. This is about twice the extent of the circular annulus reported by Lasker in 1980. That structure reported by Lasker lies in the apparently empty center of the remnant in these images.

The innermost bright knots which display strong Hα emission can be roughly fit with an ellipse. In Figure 7 an ellipse is superimposed on the Hα contours and simultaneously on the [O III] contour plot. A circle is also fitted that shares a common center with the ellipse. The circle fit is constrained mainly by the southeast quadrant of the remnant and has a diameter of 130″ (31 pc). When the center location constraint is relaxed, a simple circular fit to the remnant still produces a diameter of about 130° but the overall fit is poor. The relaxed circle center is offset by 8″.2 from the ellipse center. The ellipse is 60″ (~14 pc) along the major axis and 35″along the minor axis. The aspect ratio 0.6 suggests that the slow-moving ring is inclined at about 53° to the plane of the sky, if it is circular. This slow-moving ellipse of material would then correspond to the QSF of Cass A.

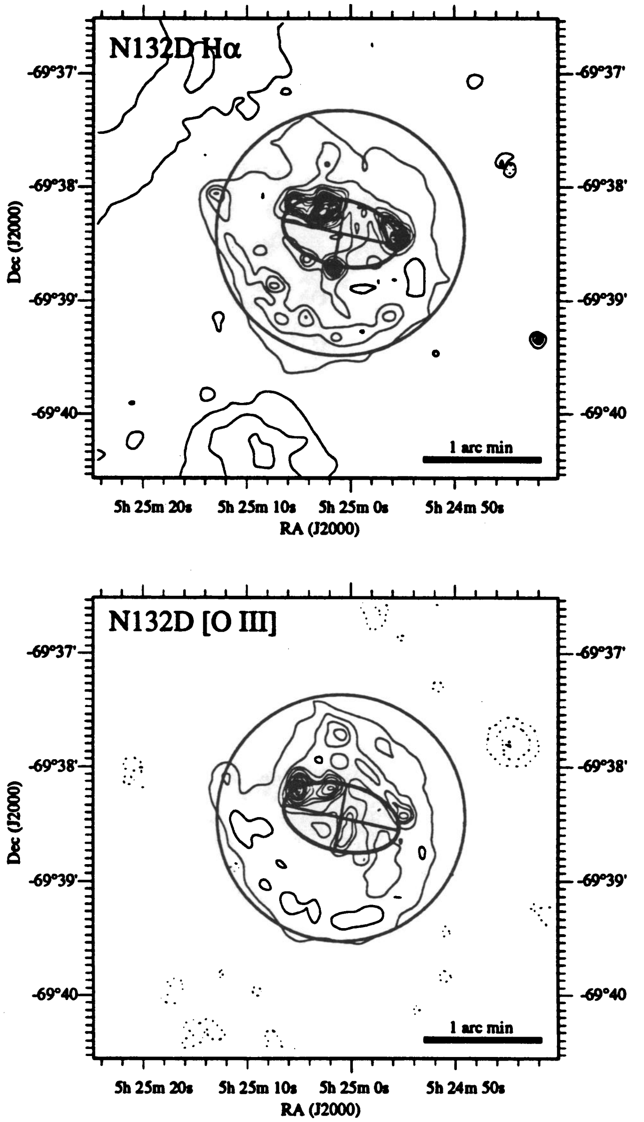

FIG. 7.—Projected geometry of N132D. In these figures, an ellipse has been superimposed on the inner bright knots of the Hα emission, corresponding to the slow-moving normal composition material. The ellipse is 60″ by 35″ and rotated 104° from the north-south line. The center is at R.A. $05^h25^m01^s$, decl. −69°38′25″. A circle fixed to this center can fit the outer remnant shock front to the southeast with a diameter of 130″.

Under the observing conditions experienced here it is doubtful whether the bright knots have been fully resolved. Spectrophotometric apertures defined by the bright knots in the imaging and two-dimensional spectrophotometry program often included two or three velocity components within a spectrum.

3.1.2. *Two-dimensional Spectrophotometry*

A velocity map was constructed using nine 600 km s^{-1} velocity bins, centered around the velocity of the slow-moving normal composition material. This is shown in Figure 8. The three middle bins (4, 5, and 6) show emission largely excluded from the Lasker analysis. Features that display spectra of oxygen-rich material are labeled "O." Material with emission

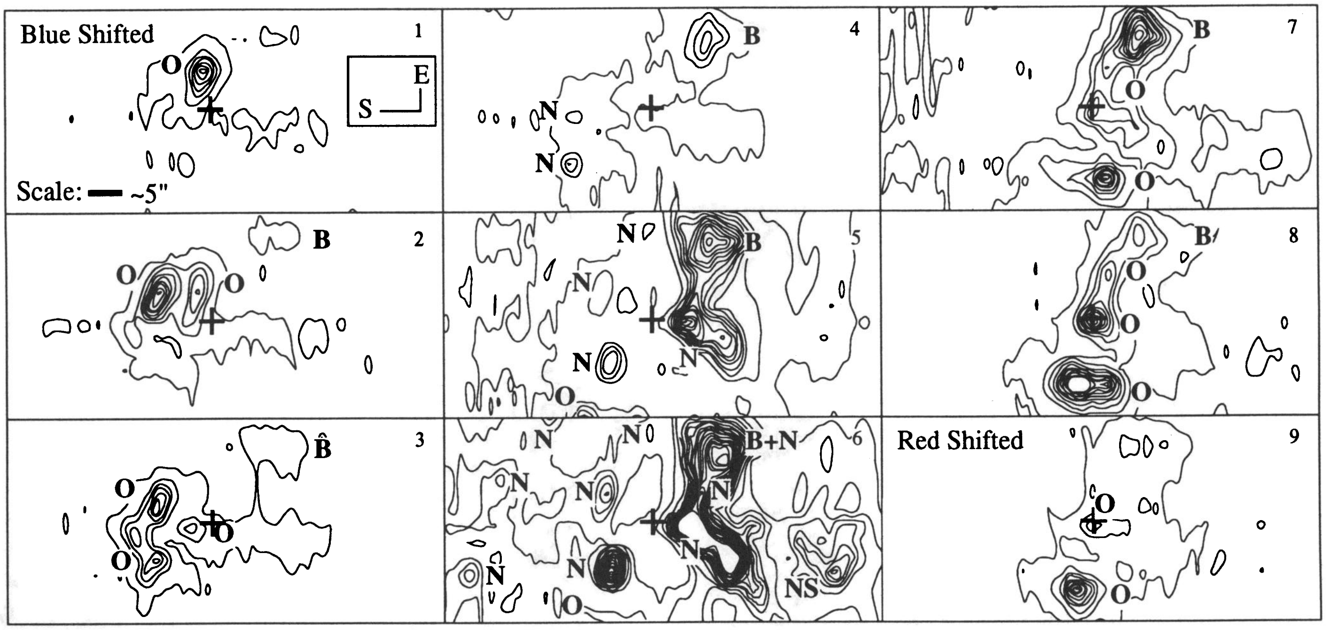

FIG. 8.—Velocity map for the inner regions of N132D in the [O II] λλ3727 line. This velocity map shows the rapidly moving oxygen-rich material in the innermost regions of the remnant that were excluded by the narrowband [O III] filter used to produce Fig. 4. The small cross is close to the center marked by Mathewson et al. (1983) and corresponds closely to the center of the ellipse in Fig. 7.

that included Hα are labeled "N." Finally a feature, designated the "broad-line" cloud, which showed very broad oxygen and neon emission lines is labeled "B."

In comparison with the Hα image, this map shows that rapidly moving oxygen-rich material exists throughout the central regions. The "arc" features noted by Mathewson et al. (1983) are not the complete tally of the oxygen-rich material. The high velocity of some material has shifted its [O III] λ5007 emission out of the filter passband. Some knots of apparently normal composition material in the narrowband images also display superimposed high-velocity blueshifted oxygen-rich material here. The eastern region of blueshifted material was not recorded in the CCD images. Significantly, the circular ring structure for the high-velocity oxygen-rich material found by Lasker (1980) is not at all obvious in the present [O II] line data. The only "ring" structure is the incomplete ellipse of normal composition low-velocity material seen earlier in the CCD images.

This velocity map observation demonstrates that the highest velocities occur in the central region, which appears to be fairly devoid in the narrowband imaging reported in the previous section. The true extent of the oxygen-rich material is now apparent and fills a broad swathe from the northeast to the southwest, about 25″ wide and 60″ long. It is not clear whether a hollow ring or ellipse geometry would provide a good fit. However, the width of the region, around apertures 4–6 and 9–12, roughly corresponds to the size of the 6 pc diameter ring of Lasker.

This information was combined with the CCD images to define the final apertures for the spectra extraction. The complete set of apertures is indicated in Figure 9 where the aperture positions are overlaid on a gray-scale image formed by co-adding both the pure emission Hα and [O III] images in a single, monochrome image.

3.1.3. *The Broad-Line Cloud*

An interesting feature detected in this observation is the broad-line oxygen emission feature, coincident with a bright knot of slow, normal composition material. This broad-line cloud is apparent in the individual spectrum as a broad component in the oxygen and neon lines of the spectrum of this knot. This is shown in Figure 1*d* where the normal spectra from an adjacent knot has been normalized on the narrow Hβ line and overlayed. The hydrogen, sulfur, and nitrogen lines overlay nearly exactly, and only the oxygen and neon features display broad lines. This knot (B) shows clearly on the velocity map over several thousand km s^{-1}. This feature appears to be an example of a direct interaction of the supernova ejecta with circumstellar material. This would occur if a large cloud of

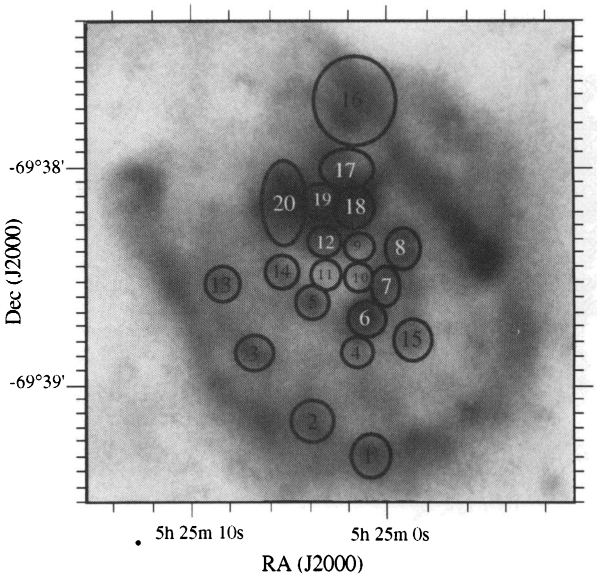

FIG. 9.—Aperture identifications for N132D. The apertures chosen for the extraction of individual spectra are shown superimposed on a gray-scale version of the composite [O III] and Hα image in Fig. 6. The central apertures 9–12, chosen from the [O II] velocity map, lie in an apparently empty region of the narrowband images due to the high velocity of the material there.

oxygen-rich material has collided with a slow-moving cloud in front of it and is now being deflected outward and around the obstacle.

3.1.4. *The Oxygen-rich Velocity Ellipse*

The oxygen-rich material detected in the apertures of Figure 9 can be used in an expansion age analysis. Radial velocities relative to the slow-moving material were measured with the [O II] λλ3727 lines for each velocity component. Some of the measured velocities are given in Tables 3A and 3B. The others are simply given in the plot. This aperture selection avoids the exclusion of low-velocity material that affected the Lasker (1980) analysis. For instance, the oxygen-rich emission in aperture 15 is of low velocity and would have been excluded in the earlier work. This knot appears a strong green knot in the composite image (Fig. 6) and is clearly oxygen-rich. There does appear to be some contamination from faint normal composition material, but this could easily be a superposition, and the remaining lines are typical of the oxygen-neon line rations of oxygen-rich material, with strong [O II] λλ3727 and [O III] λ4363.

Velocities from apertures 4, 5, 7–12, 14, 15, and 20 were measured and plotted as a function of distance from the center of the fitted ellipse of § 3.1.1. A velocity ellipse was fitted to the outer envelope of the admittedly small number of points in Figure 10.

An upper upper value of 5310 km s^{-1} is estimated for the zero-point velocity range, and a relative error of about 500 km s^{-1} in this value was also estimated. Allowing a generous 5″ radius error in the center position on a maximum extent of 26″ gives 6.2 ± 1.2 pc. This value is determined largely by the broad-line cloud in aperture 20 and the slow material in aperture 15. Apertures 5 and 14 also lend support to this radius, but they both lie in the same quadrants. The apertures 15 and 20 are opposite each other, constraining the center and radius quite well. The center lies directly between apertures 8 and 9. The smaller 14″ radius of the Lasker (1980) analysis contains the emission from apertures 7–12 in the plot.

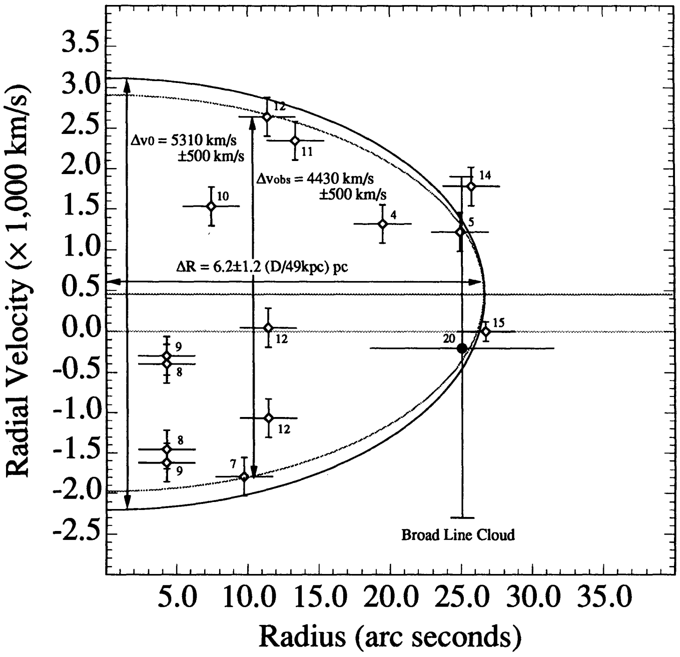

FIG. 10.—N132D oxygen-rich velocity ellipse

If the oxygen-rich material is all expanding steadily from a common origin, then the expansion age of the material is estimated at 2350 yr with a relative error of ±520 yr, found by

TABLE 3A

N132D LINE FLUXES (I_{5007} = 1.00)

Transition		Spectrum[a]					
		7v−	8v−	8v0	9v−	9v0	10v+
[OII]	λλ7320+30	0.09	0.11	...	...	...	...
[SII]	λ6731	...	...	...	...	...	...
[SII]	λ6717	:0.01	...	...	...	...	...
[NII]	λ6584	...	...	...	...	...	...
Hα	λ6563	...	...	...	...	...	...
[NII]	λ6548	...	...	...	...	...	...
[OI]	λ6300	:0.02	0.05	...	...	...	...
[OIII]	λ5007	1.00	1.00	0.30	1.00	0.36	1.00
[OIII]	λ4959	0.38	0.35	0.09	0.39	0.10	...
Hβ	λ4861	...	...	...	...	...	...
HeII	λ4686	...	...	...	...	...	...
[OIII]	λ4363	0.04	0.04	...	...	...	...
[NeIII]	λ3968	0.06	...	...	...	...	...
[NeIII]	λ3869	0.12	0.04		0.11	0.05	...
[OII]	λλ3727	1.66	1.75	0.36	1.82	0.36	1.63
$\log(I_{5007}/I_{3727})$		-0.22	-0.24	-0.07	-0.26	0.00	-0.21
$\log(I_{3727}/I_{6300})$		2.02	1.56	...	...	...	...
$\log(I_{4363}/I_{5007})$		-1.41	-1.39	...	...	...	...
$\log(I_{3869}/I_{5007})$		-0.92	-1.36	...	-0.94	-0.84	...
$\log(I_{7325}/I_{3727})$		-1.27	-1.19	...	...	...	...
Rad. Vel. [b] (km s^{-1})		-1790	-1460	-400	-1620	-300	+1540

NOTE.—Colons preceding figures indicate uncertain values.

[a] Where multiple velocity components are observed individual components are denoted by v+, v0, and v−, meaning blueshifted, rest, and redshifted, respectively.

[b] At 3727 Å using [O II] λλ3727.

TABLE 3B

N132D LINE FLUXES (J_{5007} = 1.00)

Transition		Spectrum[a]					
		11v+	12v−	12v0	12v+	14v+	15
[OII]	λλ7320+30	...	...	...	...	...	...
[SII]	λ6731	...	...	...	...	...	:0.04
[SII]	λ6717	...	...	...	...	...	:0.01
[NII]	λ6584	...	...	...	...	...	...
Hα	λ6563	...	...	...	...	...	0.16
[NII]	λ6548	...	...	...	...	...	...
[OI]	λ6300	0.05	...	...	0.07	0.05	...
[OIII]	λ5007	1.00	1.00	0.44	...	1.00	1.00
[OIII]	λ4959	0.32	0.45	0.34	...	0.34	0.43
Hβ	λ4861	...	...	...	...	...	...
HeII	λ4686	...	...	...	...	...	...
[OIII]	λ4363	:0.03	...	...	...	:0.02	0.04
[NeIII]	λ3968	...	...	...	...	...	...
[NeIII]	λ3869	0.07	...	...	...	0.11	0.16
[OII]	λλ3727	1.43	1.34	0.34	0.34	1.57	2.11
$\log(I_{5007}/I_{3727})$		-0.16	-0.13	0.11	...	-0.20	-0.32
$\log(I_{3727}/I_{6300})$		1.46	1.28	...	0.69	1.51	...
$\log(I_{4363}/I_{5007})$		-1.59	...	...	...	-1.62	-1.36
$\log(I_{3869}/I_{5007})$		-1.17	...	...	...	-0.95	-0.81
$\log(I_{7325}/I_{3727})$		...	...	...	...	...	...
Rad. Vel.[b] (km s^{-1})		+2350	-1070	+50	+2640	+1790	-200

NOTE.—Colons preceding figures indicate uncertain values.

[a] Where multiple velocity components are observed, individual components are denoted by v+, v0, and v−, meaning blueshifted, rest, and redshifted, respectively.

[b] At 3727 Å using [O II] λλ3727.

adding the measurement errors in quadrature. This is significantly larger than the 1300 yr given by Lasker (1980). This has implications for the cavity environment model discussed later.

A zero-point offset from the slow-moving material is seen here and was also noted by Lasker. This suggests that the oxygen-rich material has not been perfectly spherically ejected, with a net systemic velocity of $\sim$400 km s^{-1} compared to the bulk of the SNR. Unfortunately, the number of points is so small that no definite conclusions about symmetries in the explosion can be made. The overall velocity field is not consistent with any special expansion geometry, such as a coherent ring.

3.2. *Spectra*

Of the apertures defined in Figure 9, only the apertures containing possible oxygen-rich spectra are discussed in the following sections. The spectra from apertures 6, 7, 8, 19, and 20 are shown in Figures 1*a*–1*d*, and most of these have oxygen-rich material. Aperture 6 is included as a comparison spectrum representing the normal composition slow-moving material.

3.2.1. *Interstellar Reddening Constant*

The normal logarithmic reddening constant formalism is used in the present work where $I = I_0 10^{cf(\lambda)}$. The observed intensity for a given line is given by I, the original intensity is I_0, $f(\lambda)$ is the reddening curve (Kaler 1976), and c is the reddening constant. The curve of Kaler (1976) is based on the Whitford (1958) curve. When reddening has been expressed in other works in terms of A_v extinction or $E(B-V)$ color excess, these have been related to c approximately by

$$c \approx 1.44E(B-V) \approx 0.464A_v \; . \quad (1)$$

For N132D, spectra of some of the normal composition filaments were used to determine a reddening constant for that remnant of $c \approx 0.2$, using the observed Balmer decrement line ratios. This is consistent with normal reddening values determined for the LMC and is the same as the value given by Danziger & Liebowitz (1985). As was also noted by Danzinger & Liebowitz, some of the slow-moving filaments display steep Balmer decrements. This could be due to partially ionized shocks, known to produce steep Balmer decrements due to collisional excitation effects. Those spectra were not used for the reddening determination.

3.3. *A Dynamical Model*

The velocity map of N132D reveals a number of significant features. Firstly, the normal composition material in the N132D remnant all displays low radial velocity, while the oxygen-rich material is almost exclusively of high velocity, except at the periphery of the expansion region as might be expected. Furthermore, as may be seen in the velocity map, the oxygen-rich material is often spatially superimposed on material of more normal composition. This occurred not only for the obvious broad-line feature in aperture 20, but also in apertures 4, 5, 9, 11, 14, and possibly 15 as well. This represents the majority of the oxygen-rich knots and lends support to a model where the excitation is the result of direct interaction of the fast-moving oxygen-rich material and the slow-moving, visible, normal composition material.

More specifically, the oxygen-rich material does not appear to form an expanding circular ring structure as was suggested by Lasker (1978, 1980), but is found throughout the central regions of the remnant. The broad-line cloud, marked by B in Figure 8, is incompatible with a simple expanding ring model. The most coherent structure in the remnant is formed by the low-velocity normal composition material with spectra like those shown shown in aperture 6 (Fig. 1*a*).

Based on these observations, a simple qualitative model is proposed for this remnant to explain the remnant structure as currently observed. The ellipse of normal composition material represents the remains of a ring nebula, possibly produced in a dense stellar wind phase of the progenitor's evolution such as seen in WN ejecta-type ring nebulae. The expansion of the main SN blast wave has partially disrupted this material, leaving behind only the densest knots rather than a complete ring or shell. The oxygen-rich ejecta are expanding ballistically in all directions, and interacting with reflected bow shocks from the circumstellar nebula knots or colliding directly with the circumstellar material.

The X-ray work by Hughes (1987) suggested that the SNR is expanding into a low-density cavity. Hughes used the discrepancy between the age of 1300 yr due to Lasker (1980) and the 4000–7000 yr age derived from the X-ray observations to conclude that the outer blast front at 16 pc radius from the center has not decelerated and is still expanding at least 12,000 km s^{-1}. A very low density cavity environment was proposed to account for this. The age of $\sim$2300 yr derived here gives a somewhat lower mean blast-front velocity of 6700 km s^{-1}. Thus some deceleration may have occurred, and the very low density cavity argument is weakened, but not ruled out, since age is still significantly lower than the age that the X-ray Sedov solution gives.

Further evidence that N132D has not yet achieved the Sedov expansion phase is given by Australia Telescope 3 and 6 cm radio observations by Dickel & Milne (1993). The preliminary polarization results show that the magnetic field in the remnant is largely radial. This is usually interpreted as being characteristic of young SNR in the pre-Sedov stages of dynamical evolution. If this is the case, then this supports the cavity environment hypothesis, allowing the remnant to remain dynamically young by not having swept up a significant amount of interstellar medium after a period of 2300 yr.

We therefore propose a model of N132D with a W-R star progenitor to provide a large low-density cavity and a small ring nebula environment, with which the supernova ejacta are continuing to interact. This model would then give a natural explanation for the range of velocities observed in the SNR material. The ejecta are simply freely expanding in all directions until they encounter density contrasts in the inner regions due to the ring material. The broad-line cloud is a case where a larger cloud of oxygen-rich material straddles a slow-moving knot. Finally, the outer blast wave is continuing to expand rapidly into a low-density cavity and has therefore not been decelerated into the dynamical Sedov expansion phase.

The model structure is summarized in Figure 11.

4. PUP A AND SNR G292.0+1.8

4.1. *Observations*

In this study of Pup A, spectra of 20 individual filaments have been obtained. Eight of the slit positions revealed classical oxygen-rich material, including the "Omega" filament, and are discussed here. Other spectra taken, particularly in the northwest of the remnant, displayed unusual spectra with very strong emission of [N I] and [N II]. This is almost certainly due to actual nitrogen enhancements in that material, and a full presentation of that data will be made elsewhere. In some of the oxygen-rich spectra faint lines of species other than oxygen and neon have also been observed, including nitrogen and sulfur. This poses some problems for interpretation, but these spectra are not examined in detail in this study.

The Pup A remnant offers the opportunity to observe individually resolved filaments without the confusion in velocity space seen in N132D. The SNR G292.0+1.8 observation represents the other extreme, where only a global spectrum of the remnant is obtained and the lines are broadened by the entire velocity range of many unresolved oxygen-rich clouds.

An [O III] Schmidt plate was used as a finding chart for Pup A (a part of which is reproduced in Fig. 12). This plate was obtained for Dopita on 1983 March 25 with the UK Schmidt 48 inch (1.2 m) camera, in a 240 minute exposure through an [O II] interference filter. Several [O III] knots were identified in addition to the bright "Omega" filament of Winkler & Kirshner (1985) and the filaments of Winkler et al. (1988) The filaments are identified in Figure 12 and listed in Table 2. The figure also shows the proper-motion center obtained by Winkler et al. (1988). It is tantalizingly close to the small group of circular arcs at around R.A. $8^h22^m42^s$, Decl. $-42°59'15''$ (J2000) with a diameter of about 2′. These arcs have already been noted by Winkler et al. (1989) and have been suggested as possibly being a second SNR embedded within the Pup A bubble. This suggestion is based on the lack of separate X-ray or radio emission from this region. The arcs are highly chemically inhomogeneous and contain strong and spatially segregated nitrogen, oxygen, and sulfur emission. The proximity to the proper-motion center suggests that the arcs are in some

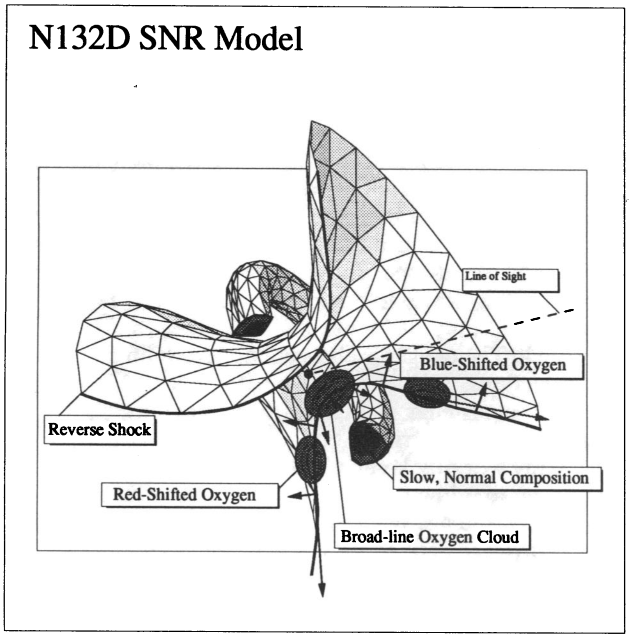

FIG. 11.—Structural model for the OSNR N132D. The observed oxygen-rich material is expanding and interacting with density discontinuities in the remnant medium. The "reverse shock" indicated here is intended to represent reflected shocks either from the blast wave itself or other secondary shocks. The slow-moving material (cf. the QSF of Cas A) may lie in a ring nebula and be providing reflecting surfaces for the shock waves. This model can provide a natural explanation for the broad-line knot as a large mass of oxygen-rich material collides with a cloud of normal material.

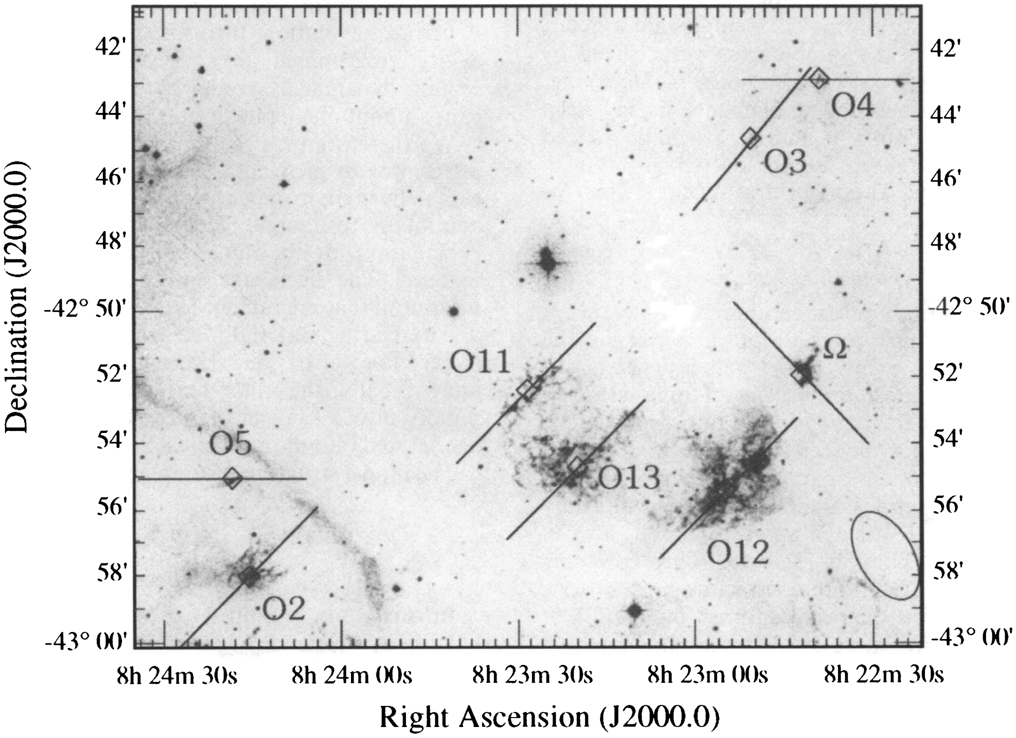

FIG. 12.—Slit positions for Pup A. The positions, size, and position angles of the observed slit positions for oxygen-rich filaments in Pup A are overlaid on the [O III] finding chart of Dopita (1989). The oval represents the proper motion center derived by Winkler et al. (1988).

way associated with the Pup A remnant itself, perhaps associated with whatever remains of the progenitor star. Spectra of these central arcs were obtained and will be presented in a future study. They are not strictly oxygen-rich, containing sulfur and, importantly, nitrogen emission, indicating that they are probably not from deep layers of the progenitor.

Using the Australian National University (ANU) 2.3 m ATT DBS PCA system described earlier, individual knots were observed with exposures ranging from 2000 to 3000 s. Multiple observations were made of the bright Omega filament in particular, totaling some 7000 s of integration. The spectra obtained of the Omega filament and slit positions O11, O12, and O13 are shown in Figures 2*a*–2*d*. The measured fluxes and ratios have been summarized in Tables 4A and 4B. Even with the extended integration, no new faint lines were identified in the Omega filament. No emission due to magnesium, argon, or calcium was detected in the oxygen-rich material, suggesting that the material from the deepest layers has not been extensively mixed with the observed oxygen-rich material. Detailed emission models would however be necessary to place a significance on this result.

The center-filled SNR G292.0+1.8 (Goss et al. 1979) suffers from heavy interstellar reddening along the line of sight, and it lies in a fairly crowded field. A CCD image obtained by S. D. Ryder with the ANU 1 m telescope was used to position the slit so as to avoid the brightest of the field stars. The spectrum is of relatively poor signal-to-noise ratio (S/N), but is important nevertheless as another data point in the all too small sample of oxygen-rich spectra.

The SNR G292.0+1.8 observation was a 3000 s exposure. The spectrum is shown in Figure 3, and the reduction was carried out concurrently with the Pup A observations. The measured fluxes and ratios are summarized along with the Pup A results in Table 4B.

4.1.1. *Reddening*

The galactic remnants suffer from quite strong and/or patchy reddening. The lack of Balmer emission lines makes it difficult to determine the reddening for individual oxygen-rich knots in Pup A, and values for nearby knots with Balmer lines may not be appropriate. Ratios derived from oxygen lines alone are fraught with modeling assumptions and are not used to derive a value of c here. A value of $A_v = 1.5$ ($c = 0.7$) was estimated by Winkler & Kirshner (1985), and for the estimated distance of 2–2.5 kpc this is not unreasonable. However, the presence of dusty clouds in the region (cf. Arendt et al. 1990) is consistent with the patchy absorption across the face of this remnant. As a consequence, the reddening for the observations of this remnant remain quite uncertain on a filament-by-filament basis.

The SNR G292.0+1.8 observation does not show Balmer lines, although a reddening excess of $E(B-V) = 0.9$ ($c = 1.3$) has been quoted for the remnant (Goss et al. 1979), based on H II absorption measurements. The small apparent size of SNR G292.0+1.8 means that a single reddening constant is likely to be applicable to the remnant.

5. RESULTS

The measured line ratios have been given in raw form without reddening corrections, and line ratios are plotted here as observed. The expected trends caused by reddening effects are estimated, so that the reliability or otherwise of the ratios can be inferred. Given the estimated reddening of $c = 0.2$ for the remnant N132D and estimates from the literature for Pup A and SNR G292.0+1.8 of $c = 0.7$ and $c = 1.3$, respectively (Winkler & Kirshner 1985; Goss et al. 1979), one can use the intermediate vector of $c = 0.5$, given on the plots, to estimate the general effect of reddening with the minimum number of assumptions about each individual observation.

The spread of ratios in the diagnostic plots, particularly the I_{7325}/I_{3727} ratio in Figure 13*c*, is mostly along the reddening vectors, with considerable scatter. For the resolved Pup A observations, it is not even obvious that one reddening value is appropriate to all the knots. Interestingly, the single point that represents the SNR G292.0+1.8 remnant on these raw plots

TABLE 4A

PUP A LINE FLUXES ([O III] $\lambda5007 = 1.00$)

Transition		Spectrum[a]					
		Ω	O2	O3*a*	O3*b*	O4	O5
[OII]	λλ7320+30	0.29	...	0.30	0.30	0.26	...
[SII]	λ6731	...	0.05	0.17	...	...	...
[SII]	λ6717	...	:0.02	0.13	...	...	...
[NII]	λ6584	...	0.25	0.53	...	...	...
Hα	λ6563	...	:0.05	0.35	0.17	...	...
[NII]	λ6548	...	0.05	0.31	...	...	...
[OI]	λ6300	0.15	0.10	0.09	...	...	...
[OIII]	λ5007	1.00	1.00	1.00	1.00	1.00	1.00
[OIII]	λ4959	0.35	0.34	0.33	0.36	0.34	0.29
Hβ	λ4861	...	0.07	0.04	...	...	...
HeII	λ4686	...	0.03	...	...	...	...
[OIII]	λ4363	0.04	0.04	...	...	...	0.08
[NeIII]	λ3968	0.03	0.05	...	...	...	...
[NeIII]	λ3869	0.12	0.12	0.10	...	...	...
[OII]	λλ3727	1.19	0.68	0.92	0.55	1.69	1.16
	$\log(I_{5007}/I_{3727})$	-0.08	0.17	0.03	0.26	-0.23	-0.06
	$\log(I_{3727}/I_{6300})$	0.92	0.84	1.00	...	...	...
	$\log(I_{4363}/I_{5007})$	-1.40	-1.36	...	...	...	-1.10
	$\log(I_{3869}/I_{5007})$	-0.92	-0.91	-1.00	...	...	...
	$\log(I_{7325}/I_{3727})$	-0.61	...	-0.49	-0.26	-0.81	...

NOTE.—Colons preceding numbers indicate uncertain values.

[a] Where multiple components are observed, individual components are denoted by *a*, *b*, *c*, etc.

TABLE 4B

PUP A AND SNR G292.0+1.8 LINE FLUXES (I_{5007}) = 1.00)

Transition		Spectrum[a]						
		O11*a*	O11*b*	O11*c*	O12	O13*a*	O13*b*	g292
[OII]	λλ7320+30	0.33	...	0.33	...	0.21	...	...
[SII]	λ6731	...	...	...	0.20	0.13	...	...
[SII]	λ6717	...	...	...	0.20	0.15	...	...
[NII]	λ6584	...	1.26	0.28	1.13	...	...	...
Hα	λ6563	...	...	...	0.25	...	...	...
[NII]	λ6548	...	0.23	:0.09	0.40	...	...	...
[OI]	λ6300	...	...	0.15	...	0.13	...	0.06
[OIII]	λ5007	1.00	1.00	1.00	1.00	1.00	0.35	1.00
[OIII]	λ4959	0.33	0.35	0.35	0.33	0.33	0.10	0.34
Hβ	λ4861	...	...	...	...	...	...	...
HeII	λ4686	...	...	...	...	...	...	...
[OIII]	λ4363	...	...	...	0.06	0.04	...	0.05
[NeIII]	λ3968	...	...	...	0.05	0.05	...	...
[NeIII]	λ3869	...	0.10	0.08	0.12	0.13	0.01	0.11
[OII]	λλ3727	1.24	2.28	1.38	2.15	1.93	0.57	1.32
	$\log(I_{5007}/I_{3727})$	-0.09	-0.36	-0.14	-0.33	-0.28	-0.21	-0.12
	$\log(I_{3727}/I_{6300})$	...	...	0.97	...	1.17	...	1.35
	$\log(I_{4363}/I_{5007})$	...	...	...	-1.22	-1.41	...	-1.31
	$\log(I_{3869}/I_{5007})$	-1.00	...	-1.09	-0.92	-0.89	-1.40	-0.97
	$\log(I_{7325}/I_{3727})$	-0.57	...	-0.63	...	-0.97	...	...

NOTE.—Colons preceding numbers indicate uncertain values.

[a] Where multiple components are observed, individual components are denoted by *a*, *b*, *c*, etc.

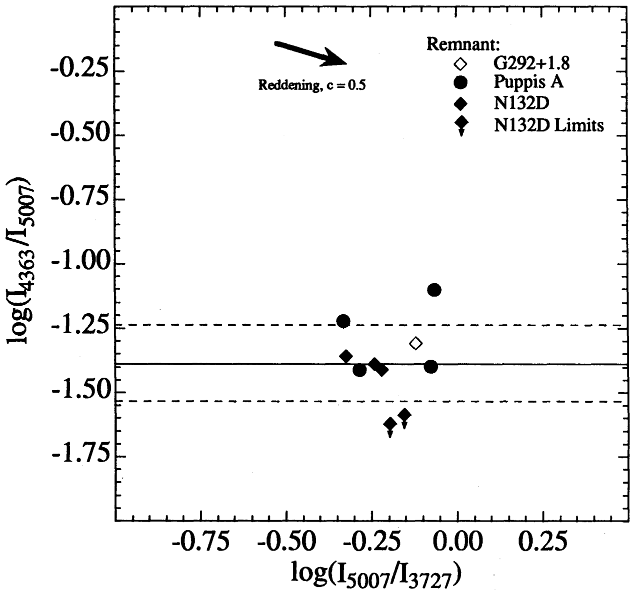

FIG. 13*a*

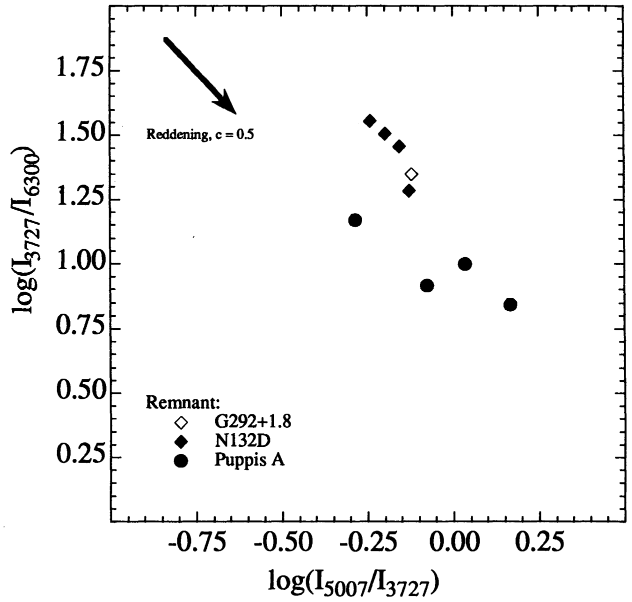

FIG. 13*b*

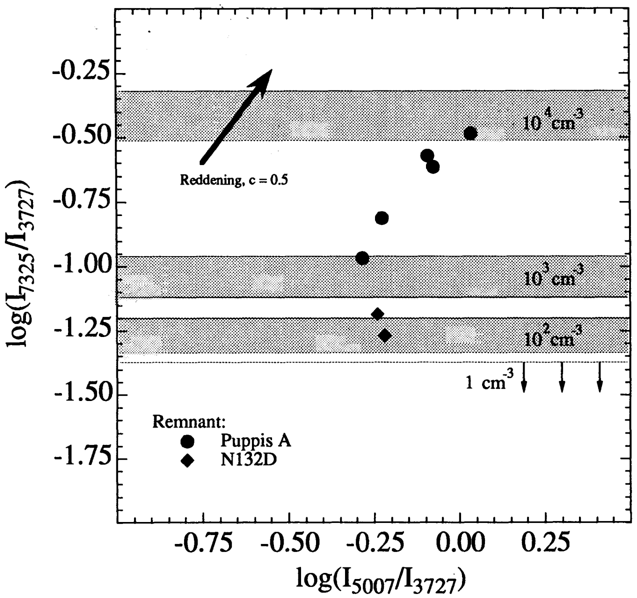

FIG. 13*c*

FIG. 13.—(*a*) This plot shows the line ratios: log (I_{4363}/I_{5007}) vs. log (I_{3727}/I_{5007}). The first ratio is a temperature-sensitive ratio, while the second is more sensitive to the density. The ratio is also sensitive to the ionization state as the normal charge exchange reactions that tie the oxygen balance to the hydrogen balance are not in effect in the oxygen-rich material. The cluster of points suggests that common conditions exist in all the observed filaments and knots. The dashed lines indicate the statistical mean value of -1.38 and a standard deviation of ± 0.15. (*b*) This plot shows the line ratios: log (I_{3727}/I_{6300}) vs. log (I_{3727}/I_{5007}). These ratios are both sensitive to ionization and density, and this plot does not have strong diagnostic powers as it is hard to separate the effects. The reddening vector also lies along the general direction of the observed correlation. There may be a vertical displacement between the N132D and Pup A points but the statistics are poor. (*c*) This plot shows the line ratios: log (I_{7325}/I_{3727}) vs. log (I_{3727}/I_{5007}). Gray bands indicate the range of the I_{7325}/I_{3727} ratio for a homogeneous oxygen-rich plasma slab model with electron temperatures of 20,000 and 30,000 K. The bands are for number densities of oxygen atoms of 10^4, 10^3, and 10^2 cm^{-3}. The low-density limit is shown for 1 cm^{-3}. If the reddening is as great as the $c = 0.5$ vector marked, then the density of the [O II]-emitting zone is most likely 10^3 cm^{-3} or less.

does not appear to be particularly reddened, tending instead to lie closer to the N132D points. Rather than dispute the heavy reddening given for this remnant, this result highlights the problems inherent in attempting to make plasma diagnostics without a detailed model for the ionization structure.

5.1. *Oxygen Line Ratios*

The oxygen line ratios for all the remnants are plotted together in Figures 13*a*–13*c*, for those spectra with sufficient lines. There are important selection effects, as the [O III] λ4363 and [O II] λλ7320+30 lines are generally only detected where they are strong, biasing the distribution of points in the plots. This should be borne in mind before any conclusions are drawn.

These plots are sensitive to the physical parameters of the emitting plasma. The [O II] λλ3727 line is sensitive to collisional quenching, so ratios of this line with other less sensitive lines such as [O III] λ5007 or [O II] λλ7320+30 give density diagnostics. The [O III] λ4363 line is a well-known temperature-sensitive line when in ratio with the [O III] λ5007 and [O III] λ4959 lines. In all the plots, the x-axis is chosen to be the ionization sensitive I_{5007}/I_{3727} ratio.

The value of the temperature sensitive [O III] I_{4363}/I_{5007} ratio (Fig. 13*a*) immediately indicates a combination of photoionization and shock heating. Normal photoionization conditions cannot generate the high I_{4363}/I_{5007} values. These would normally be less than 0.01. Shock models do not typically produce the observed I_{5007}/I_{3727} ratio either. This type of problem has features in common with the cloud-cloud collision emission mechanism studied in Sutherland, Bicknell, & Dopita (1993). An interpretation based on either a pure shock or a photoionization model is rendered even more untenable when the composition of the plasma is taken into account. Modeling by many authors since Dopita, Binette, & Tuohy (1984) (i.e., Dopita 1987; Borkowski & Shull 1991) show that the oxygen-rich plasmas have photoionization equilibrium temperatures which are much lower than normal composition photoionization, exacerbating the [O III] λ4363 flux deficit. In contrast, the pure shock models in this type of plasma produce *too much* [O III] λ4363 radiation.

The scatter in this plot is not very great in the vertical direction. This result should not be strongly affected by uncertainty in the reddening. All three remnants appear to display similar line ratios, both in their density and temperature-sensitive ratios, suggesting a common mechanism of excitation.

The mean log (I_{4363}/I_{5007}) is calculated as -1.38, with a standard error in the mean of 0.05 and a standard deviation of 0.15. If interpreted in terms of a homogeneous single-slab model, this ratio would correspond to a mean electron temperature of 22,250 K in the low-density limit, with a range from 18,000 K to 29,000 K. Such a simple interpretation is unlikely to be valid. The lower limit for reliable detection of the [O III] λ4363 line in these spectra is log $(I_{4363}/I_{5007}) \approx -1.50$. Thus, although the points do seem to cluster around -138, lower values may in fact be more common but are not detected here. The very high values, outside the standard deviations, are the most reliable measurements and do not reflect simple measurement errors. In summary, while a number of points occur at $y \approx -1.4$, this does not exclude the possibility of a wider range of physical conditions actually occurring in reality.

The next plot (Fig. 13*b*) considered combines all three observed stages of ionization of oxygen. In normal cosmic plasmas, change-exchange reactions tie the oxygen ionization balance strongly to the hydrogen balance. In the plasmas considered here, it is not known whether other charge-exchange reactions take place, such as oxygen-neon reactions, and no atomic data exist yet to model them even if they do occur. With this in mind, the plot can be considered to be sensitive to both the ionization state of the plasma and the density. This weakens the plot as a diagnostic tool for determining unique plasma properties. However, the scatter is not too great, and although there is some spread along the reddening direction, there does seem to be some remaining vertical separation between the N132D and Pup A remnants implying a difference in temperature and/or density. The previous result on temperature suggests that some of the scatter here is density related.

The final plot (Fig. 13*c*) shows I_{7325}/I_{3727} on the vertical axis, with the I_{3727}/I_{5007} ratio along the horizontal, as in previous plots. The I_{7325}/I_{3727} ratio is a density-sensitive ratio. The points on this plot display a clear correlation with a smaller scatter than the previous plots. Care should still be taken however, as the trend is also in the direction of the reddening vector. Given this caveat, this plot also supports the view that the Pup A filaments may have higher densities than the N132D filaments, although the number of knots where the red [O II] lines have been measured is small. The spread along the observed trend implies either patchy reddening or a range of densities.

In the temperature range of (2–3) × 10^4 K, the I_{7325}/I_{3727} ratio is quite a good density diagnostic, while remaining somewhat sensitive to temperature. For a homogeneous model, the density may be estimated for a given temperature. The density behavior of the I_{7325}/I_{3727} ratio has been calculated with a single-slab, oxygen-rich model at 20,000 K and 30,000 K. The results are shown as horizontal gray bands in the plot. These bands indicate the resulting temperature spread of the ratio, in density models, for decades of particle number densities. The bands are for oxygen ion densities of 10^2, 10^3, and 10^4 cm^{-3}. The lower line shows the low-density limit. While such a homogeneous model is clearly too simplistic, it seems reasonable to assume that the [O II]-emitting zones have densities somewhat less than 10^4 cm^{-3}, possibly less than 10^3 cm^{-3} if reddening is moderate or heavy in the Pup A knots. More precise estimates than this approximate limit are unjustified until a consistent model for the ionization and density structure has determined.

This less than 10^3 cm^{-3} density is quite low and suggests that much of the [O II] radiation does *not* come from the cooling zone of a shock structure. The oxygen-rich shocks in particular display enormous compression factors (10^3–10^4 or more) even with magnetic field support at microgauss levels. Any reasonable precursor density will result in much higher densities in the [O II]-emitting zones than is seen here. This is a result of isobaric cooling from the very large shock jump temperatures, which are in turn due to the large mean particle mass in the plasmas.

Tables 3 and 4 in the previous section give all the relative line fluxes detected for each aperture in each remnant in turn, many of which cannot be plotted here due to nondetections, mostly in the [O II] λλ7320 + 30 lines.

5.2. *Neon Lines*

The [Ne III] λ3869 line is the most commonly observed line apart from the oxygen lines, and it is present in most of the spectra. Importantly, the [Ne V] λ3426 line was not detected, indicating that it has an intensity significantly less than the observed [Ne III] lines in all cases. This may place constraints on the range of velocities allowable in any shock modeling. This constraint is independent to some degree of constraints that may be derived from the oxygen lines.

The presence of such universal neon emission provides supporting evidence that the majority of the emitting material indeed comes from the deep oxygen-neon layers of the proposed massive progenitor stars. Neon is a species common in all the published massive stellar evolution models, at levels high enough to give the general abundance level seen across all the remnants. Without detailed models, detailed neon abundances cannot be predicted; however, based on the similar ionization potentials and excitation rates of neon and oxygen ions, it seems that the neon is reasonably abundant compared to oxygen. An oxygen-to-neon ratio of around 0.4 by number has been successful in the modeling procedures presented by Sutherland & Dopita (Paper II) and by other workers, such as Blair et al. (1989) on another remnant, SNR E102.2−7219, consistent with the stellar models.

5.3. *Hydrogen, Nitrogen, and Sulfur Lines*

In the standard nucleosynthesis evolution models of massive stars, it is only in the outer layers that hydrogen and nitrogen can survive. Filaments were detected in both N132D and Pup A which displayed hydrogen and nitrogen in various degrees. In the context of oxygen-rich plasmas, only those which also displayed strong oxygen emission are presented here.

In Pup A a more complex situation is observed. The slit positions O11, O12, and O13 lie along an apparently connected structure, which displays oxygen emission throughout. The positions toward the remnant center (O13 and O12) also display [S II] emission as might naively be expected. However, these spectra also display strong [N II] emission, and aperture O12 shows weak Hα emission (see Figs. 2*b*–2*d*). The explanation for this is not clear. Morphologically, the structure (seen poorly in Fig. 12) is suggestive of some type of surface instability. Whether this is another ring nebula remnant, or is an outer stellar layer which has been pushed out in an unstable fashion by hot oxygen-rich material (with subsequent mixing), is uncertain. A relatively weak conclusion is therefore that the sulfur is most likely of cosmic origin, like the observed nitrogen, and not direct nuclear-processed material from the deepest layers of the progenitor star.

6. SUMMARY

The observational program presented here provided some new data in the study of the class of oxygen-rich SNRs. The detailed analysis, beyond the derivation of global properties, has been deferred to Paper II. However, a number of general conclusions can aleady be drawn.

The continuum-subtracted narrowband images of N132D have revealed the extent of the remnant. A faint extension to the northwest makes the remnant appear more nearly circular. The relatively poor seeing conditions prevented detailed comparisons with earlier epoch observations. When the [O III] and Hα images are combined, the chemical inhomogeneities in the well-known inner complex are clear. The [O III] velocity map shows that this conclusion is not affected by the selection effect of the narrow filter bandpasses, which caused some high-velocity oxygen-rich material to be excluded from the CCD imaging.

A coherent structure in the low-velocity, normal composition material is proposed, and has been fitted by an ellipse with a semimajor axis of ~30″ (~14 pc). The oxygen-rich material appears distributed throughout the ellipse region. When the ellipse center is used to fit a circular geometry to the outer parts of the SNR, the southeast edge is well fitted by a radius of 65″ (15.6 pc). The northwest edge falls somewhat short of this radius. This might suggest that there is a slightly higher density in the cavity medium in that direction.

A velocity expansion analysis of the oxygen-rich material, using the same center, gives a maximum extrapolated expansion velocity range of 5310 ± 500 km s^{-1}. The detection of oxygen-rich material well outside the 6 pc diameter ring of Lasker (1980), gives a maximum 12.4 ± 2.4 pc extent here. This results in an expansion age of 2350 ± 520 yr, between the Lasker value and the rough ~3400 yr value estimated by Danziger & Dennefeld (1976a, b). The Lasker (1980) age is certainly an underestimate of the true value.

A model in which a W-R progenitor has substantially modified the circumstellar environment before the explosion is proposed for this remnant. This is based on the presence of a ring nebula, the cavity environment, and the presence of oxygen-neon–rich material, which all suggest such a massive progenitor.

The relative spectrophotometry obtained for the three remnants gives a consistent database for the sample, making spectral comparisons a little more meaningful. The spectral results for the oxygen-rich material in all three remnants shows that the observed knots may vary in density, but show a fairly consistent temperature. This suggests a common excitation mechanism in a range of knots of different densities. Quantitative estimates of the actual plasma temperatures and densities are deferred until the modeling framework is developed.

The authors would like to acknowledge the support and help of the Anglo-Australian Observatory in obtaining the CCD images. In particular K. Taylor (AAO) was instrumental in developing the observing configuration used. We would especially like to acknowledge the assistance rendered in the CCD image reduction by S. D. Ryder (MSSSO).

REFERENCES

Arendt, R. G., Dwek, E., & Petre, R. 1991, ApJ, 368, 474

Arendt, R. G., Dwek, E., Petre, R., Dickel, J. R., Roger, R. S., Milne, D. K., & Kesteven, M. J. 1990, ApJ, 350, 266

Atherton, P. D., Taylor, K., Pike, C. D., Harmer, C. F., Parker, N., & Hook, R. N. 1982, MNRAS, 201, 661

Baade, W., & Minkowski, R. 1954, AJ, 119, 206

Blair, W. P., Raymond, J. C., Danzinger, J., & Matteucci, F. 1989, ApJ, 338, 812

Borkowski, K., & Shull, J. M. 1990, ApJ, 348, 169

Braun, R., Goss, W. M., Caswell, J. L., & Roger, R. S. 1986, A&A, 162, 259

Clark, D. H., Murdin, P., Zarneki, J. C., & Culhane, J. L. 1979, MNRAS, 188, 11P

Clark, D. H., Tuohy, I. R., & Becker, R. H. 180, MNRAS, 193, 129

Clark, D. H., Tuohy, I. R., Long, K. S., Szymkowiak, A. E., Dopita, M. A., Mathewson, D. S., & Culhane, J. L. 1982, ApJ, 255, 440

Danzinger, I. J. 1983, in IAU Symp. 101, Supernova Remnants and Their X-Ray Emission, ed. I. J. Danzinger & P. Gorenstein (Dordrecht: Reidel), 193

Danzinger, I. J., & Dennefeld, M. 1976a, ApJ, 207, 394

———. 1976b, PASP, 88, 44

Danzinger, I. J., & Leibowitz, E. M. 1985, MNRAS, 216, 365

Dickel, J. R., & Milne, D. K. 1993, private communication

Dopita, M. A. 1983, private communication

———. 1987, Australian J. Phys., 40, 789

Dopita, M. A., Binette, L., & Tuohy, I. R. 1984, ApJ, 282, 142

Dopita, M. A., Mathewson, D. S., & Ford, V. L. 1977, ApJ, 214, 179

Dopita, M. A., & Tuohy, I. R. 1984, ApJ, 282, 135

Dopita, M. A., Tuohy, I. R., & Mathewson, D. S. 1981, ApJ, 248, L105

Feast, M. W., & Walker, A. R. 1987, ARA&A, 25, 345

Fryxell, B., Müller, E., & Arnett, D. 1991, ApJ, 367, 619

Goss, W. M., Shiver, P. A., Zealey, W. J., Murdin, P., & Clark, D. H. 1979, MNRAS, 188, 357

Hughes, J. P. 1987, ApJ, 314, 103

Kaler, J. B. 1976, ApJS, 31, 517

Kamper, K. W., & van den Bergh, S. 1976, ApJS, 32, 351

Kirshner, R. P., Morse, J. A., Winkler, P. F., & Blair, W. P. 1989, ApJ, 342, 260

Lasker, B. M. 1978, ApJ, 223, 109

———. 1980, ApJ, 237, 765

Lockhart, I. A., Goss, W. M., Caswell, J. L., & McAdam, W. B. 1977, MNRAS, 179, 147

Mathewson, D. S., & Clark, J. N. 1973, ApJ, 180, 725

Mathewson, D. S., Ford, V. L., Dopita, M. A., Tuohy, I. R., Long, K. S., & Helfand, D. J. 1983, ApJS, 51, 345

Oke, J. B. 1974, ApJS, 27, 21

Petre, R., Canizares, C. R., Kriss, G. A., & Winkler, P. F. 1982, ApJ, 258, 22

Rodgers, A. W., Conroy, P., & Bloxham, G. 1988a, PASP, 100, 626

Rodgers, A. W., van Harmalen, J., King, D., Conroy, P., & Harding, P. 1988b, PASP, 100, 841

Sutherland, R. S., Bicknell, G. U., & Dopita, M. A. 1993, ApJ, 414, 510

van den Bergh, S., & Kamper, K. W. 1983, ApJ, 268, 129

———. 1985, ApJ, 293, 537

Westerlund, B. E., & Mathewson, D. S. 1966, MNRAS, 131, 371

Whitford, A. E. 1958, ApJ, 63, 201

Winkler, P. F., Canizares, C. R., Clark, G. W., Markert, T. H., & Petre, R. 1981, ApJ, 245, 574

Winkler, P. F., Hearn, D. R., Richardson, J. A., & Behnken, J. M. 1979, ApJ, 299, L123

Winkler, P. F., & Kirshner, R. P. 1985, ApJ, 299, 981

Winkler, P. F., Kirshner, R. P., Hughes, J. P., & Heathcote, S. R. 1989, Nature, 337, 48

Winkler, P. F., Tuttle, J. H., Kirshner, R. P., & Irwin, M. J. 1988, in IAU Colloq. 101, Supernova Remnants and the Interstellar Medium, ed. R. Roger & T. Landecker (Cambridge: Cambridge Univ. Press), 65